



**Stochastic Modeling of Nanoparticle Internalization and  
Expulsion through Receptor-mediated Transcytosis**

|                               |  |
|-------------------------------|--|
| Journal:                      | <i>Nanoscale</i>   |
| Manuscript ID                 | NR-ART-03-2019-002710.R1   |
| Article Type:                 | Paper  |
| Date Submitted by the Author: | 23-Apr-2019  |
| Complete List of Authors:     | Deng, Hua; Washington State University, School of Mechanical and Materials Engineering<br>Dutta, Prashanta; Washington State University, School of Mechanical and Materials Engineering<br>Liu, Jin; Washington State University, School of Mechanical and Materials Engineering |
|                               |  |

## Stochastic Modeling of Nanoparticle Internalization and Expulsion through Receptor-mediated Transcytosis

Hua Deng <sup>a</sup> Prashnanta Dutta <sup>a</sup> and Jin Liu <sup>\*a</sup>

Received 00th January 20xx,  
Accepted 00th January 20xx

DOI: 10.1039/x0xx00000x

The receptor-mediated transcytosis (RMT) is a fundamental mechanism for the transcellular transport of nanoparticles. RMT is a complex process, during which the nanoparticles actively interact with the membrane and the membrane profile undergoes extreme deformations for particle internalization and expulsion. In this work, we developed a stochastic model to study the endocytosis and exocytosis of nanoparticle across soft membranes. The model is based on the combination of a stochastic particle binding model with a membrane model, and accounts for both the clathrin-mediated endocytosis for internalization and the actin-mediated exocytosis for expulsion. Our results showed the nanoparticle must have certain avidity with enough ligand density and ligand-receptor binding affinity to be uptaken, while too much avidity limited the particle release from the cell surface. We further explored the functional roles of actin during exocytosis, which has been a topic under active debates. Our simulations indicated that the membrane compression due to the actin induced tension tended to break the ligand-receptor bonds and to shrink the fusion pore. Therefore, an intermediate tension promoted the fusion pore expansion and nanoparticle release, while high tension prohibits particle release. Our model leads to new and critical mechanistic insights into RMT, and represents a powerful platform for aiding the rational design of nanocarriers for controlled drug delivery.

### 1 Introduction

The receptor-mediated transcytosis (RMT) is of significant importance for the understanding of the fundamental biological transportation of nutrients and viruses, as well as biomedical applications in drug delivery.<sup>1-5</sup> For example, it is well known that epithelial cells facilitate fast transcellular transport of various viruses, such as human immunodeficiency virus (HIV) influenza virus, and poliovirus.<sup>6-9</sup> RMT is also a promising and non-invasive technique for delivery of drug carriers across endothelial cells at blood-brain barrier (BBB) for brain cancer and neurodegenerative diseases, such as *Alzheimer's* disease and *Parkinson's* disease.<sup>4, 10</sup> The RMT process includes both particle internalization through receptor-mediated endocytosis (RME) and expulsion through exocytosis. Theoretical and experimental works have investigated the internalization of nanoparticles through RME.<sup>11-15</sup> But the exocytosis process during RMT has been rarely studied. Recent investigations have demonstrated that higher endocytosis may not automatically lead to a better transcytosis capability of nanoparticle.<sup>16-18</sup> The precise mechanism behind the efficient transport of nanoparticle through RMT is still less understood.

As illustrated in Figure 1, transport of nanoparticles across a cell through RMT is a complex and multi-stage process. It requires the selective binding of particle to the receptors on one side of the cell surface, internalization of the particles, transport of the vesicle through the cytoplasm, docking to the surface on the other side of the cell, fusion with the lipid membrane and eventually expulsion of the particle from the membrane. Understanding the interactions between nanoparticle and membrane and the extreme deformations of membrane during

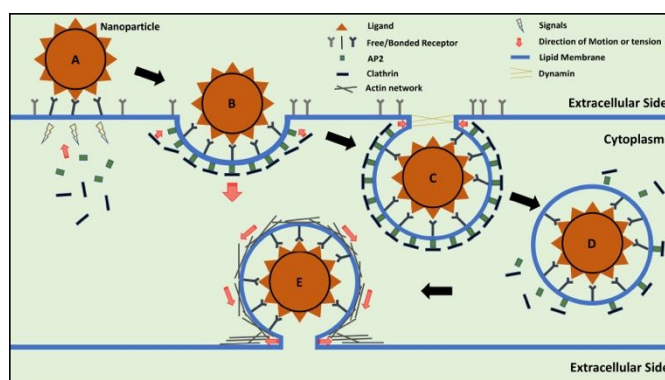


**Figure 1.** Schematic of the receptor-mediated transcytosis of nanoparticle. The particle first binds with the receptors on the extracellular side of the cell, then the interactions trigger the assembly of clathrin-coated pit (CCP). CCP induces the deformation of membrane and the formation of the particle-containing vesicle. The mature vesicle is pinched off from the membrane with the assistance of dynamin and transported to the other side. During the transportation, clathrin coats are disassembled from the vesicle surface. The exocytosis starts with the fusion between the vesicle and the cell membrane. The post-fusion pore opening is mediated by the actin network activity.

<sup>a</sup> School of Mechanical and Materials Engineering, Washington State University, WA 99163, USA

E-mail: jin.liu2@wsu.edu

† Footnotes relating to the title and/or authors should appear here.

Electronic Supplementary Information (ESI) available: [details of any supplementary information available should be included here]. See DOI: 10.1039/x0xx00000x

both internalization and expulsion is critical for the transcellular transport of nanoparticle through RMT.

Many nanoparticle properties, such as the particle size, shape, ligand density/type, etc. and biological factors, such as the assembly of clathrin and actin as mentioned above, will impact the membrane deformation during the transcytosis. Therefore, a numerical model, which is able to incorporate the effects from key biological components, is desirable for studying the receptor-mediated transcytosis of nanoparticle. The receptor-mediated endocytosis and internalization of particles have been well-characterized and a variety of computational models exist in the literature,<sup>11, 13, 19-22</sup> but the exocytosis and expulsion of nanoparticles have been less explored.<sup>23-26</sup> Alternative translocation pathways through membrane rupture and penetration have also been studied through coarse-grained molecular simulations.<sup>27, 28</sup> In this work, we developed a stochastic model for the RMT and applied this model to study the internalization and expulsion of ligand-coated nanoparticle. Our model is a combination of receptor-mediated endocytosis and exocytosis. The effects of assembly of clathrin-coated pit (CCP) and actin have been taken into account in endocytosis and exocytosis processes respectively. Using our model, we systematically investigate the effects of ligand density and ligand-receptor binding affinity on the overall effectiveness of transcytosis. In addition, we also explore the functional roles of filamentous actin assembly during fusion pore expansion and particle release. The results are consistent with available experiments and provide deeper understanding of the fundamental mechanisms involved in this complex process.

## 2 Model and Methods

### 2.1 Clathrin-mediated Endocytosis Model

In our model, the nanoparticle is treated as a rigid sphere with ligands uniformly coated on its surface. The nanoparticle is able to translate and rotate. The ligands and receptors are modeled as cylinders with one end attached to the particle/membrane surface and the other free end as binding tip. The membrane surface is modeled with Helfrich Hamiltonian<sup>29</sup> using a three-dimensional curvilinear triangulate system. The total energy  $E$  of membrane is:

$$E = \iint \left[ \frac{\kappa}{2} (2H - H_0)^2 + \bar{\kappa} K + \sigma \right] dA \quad (1)$$

where  $\kappa$  and  $\bar{\kappa}$  are the bending rigidity and Gaussian rigidity of the membrane, and  $\sigma$  represents the membrane tension.  $H = (c_1 + c_2)/2$  is the mean curvature and  $K = c_1 c_2$ , is the Gaussian curvature of the surface,  $c_1$  and  $c_2$  are the principal radii of curvatures.  $H_0$  is the intrinsic or spontaneous mean curvature of the membrane. Since the membrane has fixed topological type in our simulation, the Gaussian rigidity term remains a constant and is hence not included in the model. The tension term is included because it plays an important role in transcytosis.

During endocytosis, the clathrin coated pit is modeled as additional intrinsic curvature and modified bending rigidity. Therefore, the total energy with clathrin can be expressed as:

$$E = \iint \left[ \frac{\kappa}{2} (2H)^2 + \sigma \right] dA + \iint \left[ \frac{\kappa_{cla}}{2} (2H - H_{cla})^2 \right] dA \quad (2)$$

where  $\kappa_{cla}$  and  $H_{cla}$  are the bending rigidity and intrinsic curvature of the clathrin coat. In our model, the ligand and receptor binding trigger the recruitment of clathrin lattices; each new binding introduces a curvature field representing the accumulated clathrin. The ligand-receptor interactions are modeled by the Bell model:<sup>30</sup>

$$\Delta G_r(d) = \Delta G_0 + \frac{1}{2} k d^2 \quad (3)$$

Here  $d$  is the distance between the binding tips of the interacting ligand and receptor,  $\Delta G_0$  is the equilibrium free energy change at  $d = 0$ , and  $k$  is the interaction bond force constant. In our model,  $\Delta G_0$  is obtained from the dissociation constant  $K_d$  via  $\Delta G_0 = -k_B T \ln K_d$ , where  $k_B$  is the Boltzmann constant and  $T$  is the thermodynamic temperature. Ligand and receptor pairs are allowed to form bonds within the reaction cut-off distance  $d_c$ .<sup>31</sup> The bonds are reversible, they may break due to nanoparticle and receptor movements or membrane deformation.  $k$  will be determined from  $\Delta G_0$  and  $d_c$ . For a bonded receptor, it is allowed to bend and rotate. This flexural movement of receptor represents the entropy change during binding. Under the assumption of small deformations, we model the flexure of a receptor as bending a beam from equilibrium (normal to membrane surface) position, and the bending energy is calculated as:

$$\Delta G_f(\theta) = (2EI/L)\theta^2 \quad (4)$$

where  $EI$  is the receptor flexural rigidity,  $L$  is the receptor length and  $\theta$  represents the bending angle from the normal direction of the local membrane. Therefore, the total binding energy change for each interaction is the difference between the energy reduction by ligand-receptor interaction and the energy increase through receptor bending. More details regarding the endocytosis model can be found from our previous publication.<sup>22</sup>

### 2.2 Exocytosis Model

Our exocytosis model mimics the expansion of the fusion pore and the potential release of the nanoparticle. With the vesicle, the receptors and drug carrier are transported across the cell. During the transport, the clathrin coats have already been disassembled from the vesicle surface. Therefore, the clathrin introduced intrinsic curvature is removed from the exocytosis model.

The affinity between ligand and receptor may be pH dependent or independent. For example, the binding affinities of apo-transferrin and holo-transferrin changes under different pH values.<sup>32</sup> During endocytosis, holo-transferrins bind to the TfRs on the membrane surface at pH 7.0. The acidification of endocytic vesicle during transportation causes the pH to be

lower to 5.5, which triggers the disassociation of irons from the holo-transferrins. The iron-free apo-transferrins under acidic environment have similar affinity as holo-transferrin at pH 7.0. Therefore, the transferrins are able to keep binding with the TfRs during the transportation. There are also ligands with lower affinity at acidic condition as well as some other types of ligands with the same affinity under neutral and acidic pH values.<sup>16, 33, 34</sup> In our model, we consider ligands that are pH independent and have higher affinity with their receptors under acidic environment. This way, we can assume that there is no bond breakage during the endosome transportation. Therefore, the number of bonds and receptors at the start of exocytosis simulation is the same as at the end of its corresponding endocytosis simulation. This assumption can be relaxed in future studies. Before running the exocytosis simulation, we relax the membrane with zero intrinsic curvature while keeping all the other interactions and vesicle shape.

Filamentous actins play key roles during exocytosis.<sup>35–38</sup> The precise distribution of the actin filaments is not well established. In our model the impacts of actin are modeled as two effects as illustrated in Figure 2. First, an increased tension is applied on the vesicle (yellow region) and the neck (red region). The added tension is caused by the contractile activity of actin and myosin complexes to compress the vesicle.<sup>37</sup> As a result, the energy of the local membrane with higher surface tension becomes:

$$E = \iint \left[ \frac{\kappa}{2} (2H)^2 + \sigma_{actin} \right] dA \quad (5)$$

Here,  $\sigma_{actin}$  is the tension under the compression of actin network. In addition, we assume the distribution of the actin-myosin complexes is different at the neck region (see Figure 2). Therefore, an additional parallel force is applied to facilitate the pore opening. The magnitude of the force is assumed to be determined by the pressure  $P$  due to the actin activity at the neck and the surface area ( $A_i$ ) occupied by the vertex  $i$ . The pressure is in kPa range and assumed to be uniformly distributed.<sup>39</sup> As a result, an extra energy change of  $\Delta G_{af} = -P A_i \delta_i$  is added for a vertex movement near the neck due to the force. Here  $\delta_i$  is the distance traveled along the direction of actin force. Besides, the effects of actin induced tension and force are removed when the particle is detached from the membrane surface.

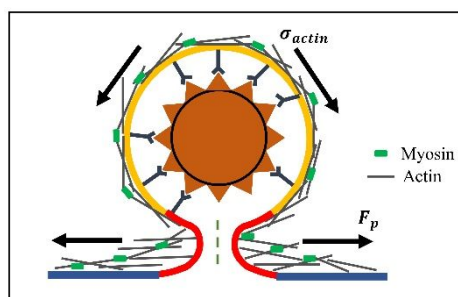


**Figure 2.** Schematic of the modeling of the filamentous actins. The effects of actin are modeled as two effects: an increased surface tension  $\sigma_{actin}$  on the vesicle and a parallel force at the neck region.

The simulation contains four Monte Carlo (MC) types: receptor diffusion, particle translation or rotation, bond formation or breakage, and membrane surface evolution. In each MC step, one of the movements will be randomly selected and the system energy ( $U$ ) is calculated for the new configuration. The  $U_{new}$  includes the membrane elastic energy  $E$ , ligand-receptor interaction energy  $\Delta G_r$ , receptor flexural energy  $\Delta G_f$  and actin force energy  $\Delta G_{af}$ . The new configuration is accepted with the following probability:  $\min \{1, \exp [-(U_{new} - U_{old})/k_B T]\}$ .

### 3 Results and Discussion

We have developed a stochastic model for clathrin-mediated endocytosis and exocytosis (see Method section). We implement our model to investigate the effects of nanoparticle avidity on the overall effectiveness of receptor-mediated transcytosis across the membrane. The avidity of a nanoparticle is determined by many factors, such as the affinity of the ligand to receptor, valence of the ligand, the ligand density and particle size/shape etc. Here two important factors: ligand density and ligand-receptor binding affinity, have been explored. Throughout our simulations, the particle size has been fixed at 80 nm. The ligand and receptor parameters have been set to mimic the transferrin (Tf) and transferrin receptor (TfR) which are known to trigger CME.

#### 3.1 Clathrin-mediated Endocytosis: ligand density effect

We first study the ligand density effect by varying the number of ligands on a particle as 30, 52, 60, 70, 80, 90, 106 and 126, corresponding to ligand density  $\rho_{ab}$  from 1500 to 6300/ $\mu\text{m}^2$ . The ligand-receptor interaction parameters are chosen to mimic the transferrin-TfR interactions with  $K_d = 0.76 \text{ nM}$ . Other simulation parameters are listed in Appendix A.

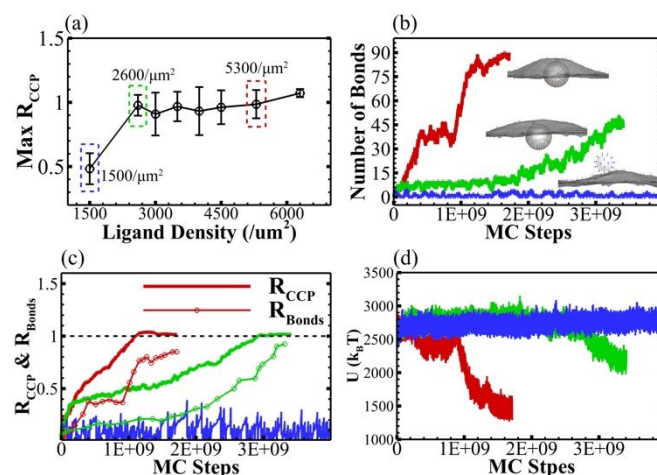


**Figure 3.** Effect of ligand density on clathrin mediated endocytosis. **(a)** The maximal CCP ratio  $R_{CCP}$  observed at different ligand densities. The standard deviation is based on 5 independent simulations. **(b)** The number of bonds change in the MC simulation for nanoparticles with high (5300/ $\mu\text{m}^2$ ), intermediate (2600/ $\mu\text{m}^2$ ) and low (1500/ $\mu\text{m}^2$ ) ligand densities. The equilibrium profiles of the membrane are also shown. **(c)** The CCP ratio (solid line) and bonds ratio (dotted line) change with MC steps. **(d)** The total energy of the system during the simulation.

As shown in Figure 3 (a), the CCP area ratio  $R_{CCP}$  is the area of CCP normalized by the area of the minimal vesicle that encapsulates the nanoparticle, ligand and receptor complex. The observed maximal  $R_{CCP}$  in the simulation first increases with the ligand density and then saturates ( $R_{CCP} \sim 1.0$ ) after ligand density  $2600/\mu\text{m}^2$ . The results are consistent with the experiments from Banerjee *et al.*<sup>40</sup> and simulations from our previous work with 100 nm particles.<sup>22</sup> The clathrin coated area directly relates to the endocytosis and indicates whether the particle is able to be internalized. For particle with low ligand density ( $1500/\mu\text{m}^2$ ), as indicated in Figure 3 (b) and (c), only a few ligand-receptor bonds form and break with small patch of CCP forms because of the bonds. The particle moves above the membrane and can never be fully internalized. With higher ligand density ( $2600/\mu\text{m}^2$  and  $5300/\mu\text{m}^2$ ), the number of ligand-receptor bonds continuously increases, and the particle firmly attaches on the membrane. A mature vesicle with clear neck regions is formed and the particle is eventually internalized as indicated in Figure 3 (c) when  $R_{CCP} \sim 1.0$ . The high ligand density nanoparticle ( $5300/\mu\text{m}^2$ ) is uptake in less MC steps. In Figure 3 (c), we also show the bonds ratio  $R_{Bonds}$  that indicates the percentage of bonded ligands over total ligands coated. As shown, both cases have similar percentage of  $R_{Bonds} \approx 0.8$  when internalized. In Figure 3 (d), the energy of the system reflects the bond forming status. The decreasing of the total energy is mainly driven by the continuous bond formation. The high ligand density nanoparticle reaches the lowest energy status due to highest number of bonds formed.

In addition, as shown in Figure 3(b), the bond formations are different for the two nanoparticles with ligand densities of  $2600/\mu\text{m}^2$  and  $5300/\mu\text{m}^2$ . There is a sudden jump of number of bonds for high ligand density nanoparticle ( $5300/\mu\text{m}^2$ ) while a much smoother bond formation for nanoparticle with  $2600/\mu\text{m}^2$ . Two factors determine the bond formation: the first factor is the membrane deformation driven by the thermal fluctuations and CCP spontaneous deformation. The second factor is the ligand density of the nanoparticle. For high ligand density nanoparticle ( $5300/\mu\text{m}^2$ ), the larger number of ligands leads to the fast growing of bonds on one half of the nanoparticle within  $\sim 5e8$  MC steps, after which the bond number reaches a short plateau. The plateau period is due to the orientation change of ligand tips at the edge of the contact region. The membrane needs further deformation to accommodate the barrier by random thermal fluctuations and CCP accumulation. After overcoming the energy barrier, the receptors are able to access the rest of ligands on the other half of the nanoparticle. Therefore, the bond number suddenly jumps again at  $\sim 1e9$  MC steps because of the high ligand density. In contrast, a smoother growing of bonds is observed for the nanoparticle with  $2600/\mu\text{m}^2$  ligand density because of the reduced number of available ligands on the nanoparticle.

The detailed evolution of the particle-membrane system is illustrated in Figure 4. As shown in Figure 4 (a), the particle with high ligand density ( $5300/\mu\text{m}^2$ ) firmly docks on the flat membrane with a few of bonds at beginning. The binding induced recruitment of clathrin lattices forms the initial clathrin

plaque under the nanoparticle. The deformation of the membrane is driven by the increased CCP due to more bindings and its spontaneous deformation. The nanoparticle is then shallowly and deeply wrapped by the gradually invaginated membrane. A mature vesicle is finally formed with CCP fully coated on the surface. The aggregation of clathrin directly drives the local membrane deformation. The clathrin coated vesicle has uniformly distributed and positive curvature. The curvature starts to reduce near the neck region and finally becomes negative at the region connecting the flat membrane. The shape of neck is consistent with the catenoid-like shape predicted in membrane fission.<sup>41</sup> On the other hand, as shown in Figure 4 (b), the low density ( $1500/\mu\text{m}^2$ ) nanoparticle can only temperately contact the membrane with few bonds. As a result, the nanoparticle moves around on the membrane with bonds frequently form and break. The area of CCP is also limited to a low value.

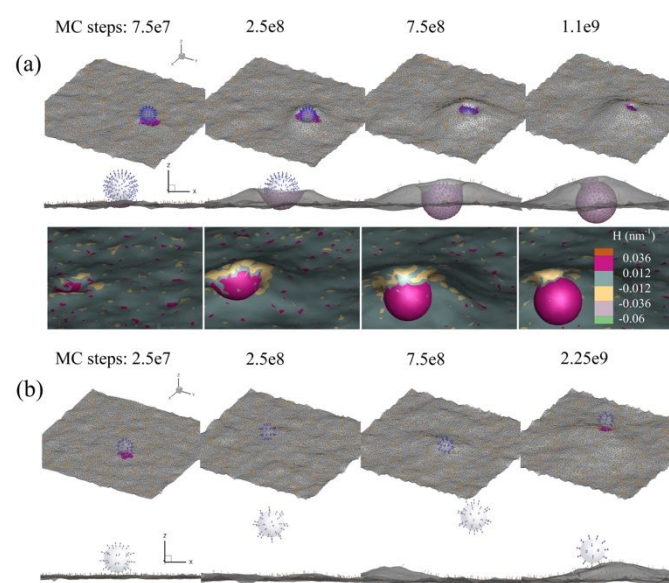


**Figure 4.** The membrane deformation and nanoparticle movement during the CME for ligand density  $5300/\mu\text{m}^2$  and  $1500/\mu\text{m}^2$  cases. **(a)** The top and side views of the membrane show fully wrapping of the nanoparticle with  $5300/\mu\text{m}^2$ . The docking of the nanoparticle to the flat membrane with initial clathrin plaque ( $7.5e7$  MC steps), shallow wrapping ( $2.5e8$  MC steps), deep wrapping ( $7.5e8$  MC steps) and complete vesicle formation ( $1.1e9$  MC steps) are observed. The contours of the distribution of mean curvature at the endocytic site are also shown from the bottom view. **(b)** The nanoparticle with low ligand density ( $1500/\mu\text{m}^2$ ) keeps moving around on the membrane. The number of bonds formed is not able to sustain the CME process. The CCP (pink region), bonded receptor (red dots), free receptor (orange dots), bonded ligand (green dots) and unbonded ligand (blue dots) are all shown in the profiles

### 3.2 Clathrin-mediated Endocytosis: ligand-receptor binding affinity effect

Another important factor determines the avidity of particle with its receptor is the affinity of the targeting ligand itself. To simplify our model, we make the assumption that the ligand is monovalent and the affinity with the receptor is unchanged during the transportation. The affinities (in  $K_d$ ) of different

ligands are commonly ranging from less than 1 to few hundreds  $nM$ <sup>16,32</sup> and the avidity of particle is able to reach  $0.01 nM$ <sup>17</sup> in experiment. Here we fix the ligand density at  $5300/\mu m^2$ , and then systematically vary the ligands binding affinity with  $K_d = 0.12, 0.32, 0.76, 0.97, 1.23, 1.73, 2.82, 6.93, 65.0$  and  $111.0 nM$ . All the other parameters are the same as in Appendix A. For simplification in our model, we assume that the reaction cut-off distance for each ligand is fixed. Thus, the equilibrium energy  $\Delta G_0$  and spring constant  $k$  in Equation (3) are adjusted according to each  $K_d$  value.

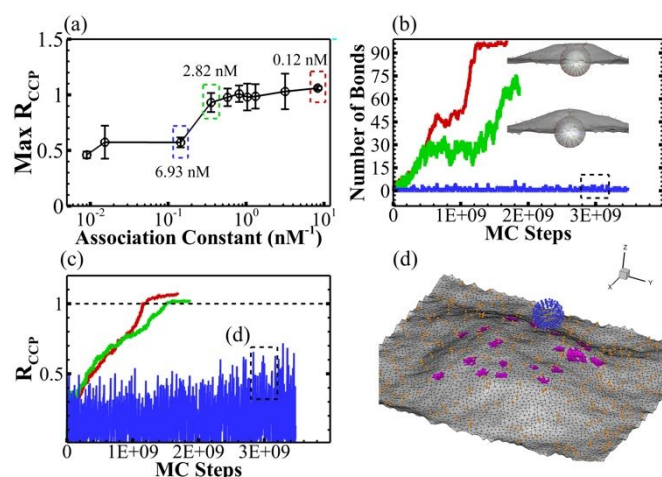


**Figure 5.** Effect of ligand-receptor binding affinity on clathrin mediated endocytosis. (a) Max CCP ratio  $R_{CCP}$  at different ligand binding affinities. The x-axis shows the association constant  $K_a$  ( $K_a = 1/K_d$ ). The standard deviation is based on 5 independent simulations. (b) The number of bonds formed during the CME. The equilibrium profiles for  $K_d = 0.12$  and  $2.82 nM$  cases are shown. (c) The CCP ratio change in the MC simulations. (d) The profile of the nanoparticle with low ligand affinity ( $K_d = 6.93 nM$ ) at around  $3.0e9$  MC steps. The nanoparticle cannot be internalized by the membrane throughout the simulation. Small clathrin plaques are randomly distributed on the membrane surface. The CCP (pink region), bonded receptor (red dots), free receptor (orange dots), bonded ligand (green dots) and unbonded ligand (blue dots) are all shown in the profile.

Figure 5 shows the effect from ligand-receptor binding affinity. As shown in Figure 5(a), similar to the ligand density effect, there is a critical affinity ( $K_d = 2.82 nM$ ) that need to be overcome to achieve complete internalization. At low ligand-receptor binding affinity, as indicated in Figure 5(b), only a few weak bonds form and break. The particle frequently moves above the membrane and triggers the forming of small CCPs at distinct positions (Figure 5(d)). Those small CCPs are disappeared shortly after the detachment of the particle. On the other hand, stronger binding affinity allows the particle to firmly attach to the cell surface and keep forming new bonds. As shown in Figure 5 (c), The area of CCP continuously increases and a mature vesicle is eventually formed. The internalized nanoparticles with  $K_d = 0.12$  and  $2.82 nM$  show  $R_{CCP} \approx 0.9$  and  $0.6$  respectively. Together with the observed  $R_{Bonds} \approx 0.8$  with  $K_d = 0.76 nM$  in the above studies (Figure 3 (c)), we find that higher ligand affinity leads to a higher ligand usage and receptor consumptions. The ligand density only determines the probability of forming a new bond while the ligand affinity determines the breakage rate of the existing bonds. The blue

lines in Figure 3 (c) and Figure 5 (c) illustrate how the two parameters determine the behaviours of the nanoparticle. The high ligand affinity but low density nanoparticle, as shown in Figure 3 (c), features a longer interval but lower CCP ratio pattern due to more stabilized bonds but lower probability to form more interactions. In contrast, the high ligand density but low affinity nanoparticle has a more frequent fluctuation with higher CCP ratio pattern due to high probability for forming unstable bonds. The CCP patches are randomly distributed on the membrane as shown in Figure 5(d).

### 3.3 Exocytosis: ligand density effect

To effectively deliver NPs across the cell, it is important not only to enter the cell but also release the cargo on the cell surface. Therefore, we also implement our model to investigate the process of exocytosis (see Method section). A common situation that requires RMT is the transportation of nanoparticles across polarized cells such as endothelial and epithelial cells. For those polarized cells, the functionality and protein expression are usually distinct between apical and basolateral membranes.<sup>42,43</sup> For example, the highly polarized distribution of TfRs on the endothelial cells of BBB is observed<sup>44</sup>. It has been proposed that the majority of TfRs are localized on the blood side membrane due to inherent recycling of endosomes. The newly synthesized immunoglobulin receptors (pIgR) are also found to be sorted to the basolateral surface of the mucosal epithelial cells. Then the secretory IgA-pIgR complex is transported to the apical surface through RMT. Finally, the proteolytic cleavage of pIgR at the apical surface ensures a unidirectional transcytosis pathway.<sup>45</sup> In our study, the transcytosis of nanoparticles may allow the receptors to bypass the recycling pathway and to be delivered to the other side of the cell. In our exocytosis model, we assume the local receptor density on our simulation membrane is determined by the receptors carried by the endocytic vesicle. This is a reasonable assumption given the extremely low receptor density on the exocytosis surface.

We first study the effect of ligand density. The initial configurations of exocytosis are selected from the end of endocytosis simulations presented in Figure 3. Three ligand densities of  $\rho_{ab} = 2600, 5300$  and  $6300/\mu m^2$  are chosen for study. The number of receptors brought to the brain side by vesicle is  $\sim 40, 90$ , and  $90$  respectively depending on the number of bonds during endocytosis. We have also run 5 independent simulations on each case and all simulations show similar results. Therefore, results shown in Figure 5 are from one of the simulations.

Figure 6(a) shows the number of ligand-receptor bonds during simulations with different ligand densities. As shown, when the ligand density is relatively low ( $\rho_{ab} = 2600/\mu m^2$ ), the number of bonds quickly drops from  $\sim 20$  to zero within  $1.0 \times 10^9$  MC steps. The particle is released from the vesicle as the number of bonds reaches to zero. The expulsion process of the particle is illustrated in Figure 6(d) at different stages. As the ligand density is increased ( $\rho_{ab} = 5300/\mu m^2$ ), as shown in Figure 6(a), the number of bonds first quickly decreases, then

fluctuates around  $\sim 20$  for a long period of simulation and finally drops to zero at  $\sim 2.0 \times 10^9$  MC steps. The particle eventually leaves the vesicle as illustrated in Figure 6(d). When ligand density is further increased to high level ( $\rho_{ab} = 6300/\mu\text{m}^2$ ), the number of bonds first rapidly drops and then reaches equilibrium value  $\sim 20$ , but never goes to zero. As shown in Figure 6(d), in this case, there are always certain number of ligand-receptor bonds at the bottom keeping the particle attached on the membrane. We also measure the diameter of the pore near the neck region of the vesicle. Figure 6(c) illustrates the bottom view of the membrane and how the pore diameter was measured. The membrane pore opening is determined by the combined effects of membrane tension, actin forces and local binding situation. Figure 6(b) shows the pore diameter evolution as a function of MC steps. As shown, for all cases studied here, the actin force is able to open the fusion pore large enough for the release of the particle. After that, the avidity of the particle determines whether the particle is able to leave the vesicle or not. When the ligand density is high, the particle remains attached on the membrane which slows down the opening of the fusion pore. On the other hand, for  $\rho_{ab} = 2600/\mu\text{m}^2$  and  $5300/\mu\text{m}^2$  cases, the particles are released from the vesicle and the vesicle eventually merge with the flat membrane. As a result, the pore diameters show similar trends for these two cases.

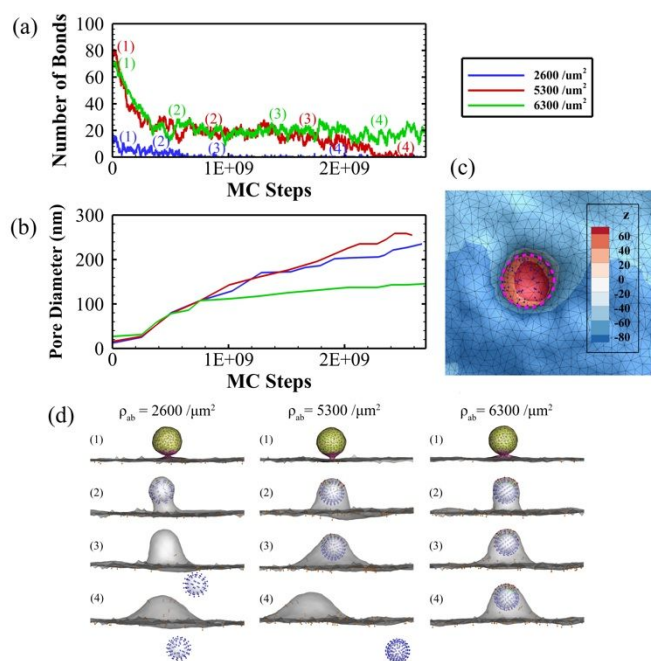


**Figure 6.** Effect of ligand density on exocytosis. (a) The number of ligand-receptor bonds formed during the MC simulations. (b) The diameter of the fusion pore during the simulations. (c) The ring of the vesicle neck (dotted pink ring) after fusion with the membrane. The contour shows the z-coordinates (in nm) of the vertices from a bottom view. (d) The evolution of the profiles of the membrane-particle system at ligand density of  $2600$ ,  $5300$ , and  $6300/\mu\text{m}^2$ . The actin induced tension (yellow region), actin induced force (pink region), bonded receptor (red dots), free receptor (orange dots), bonded ligand (green dots) and unbonded ligand (blue dots) are all shown in the profiles.

### 3.4 Exocytosis: ligand-receptor binding affinity effect

To show the effect of ligand-receptor binding affinity on exocytosis, we fix the ligand density at  $5300/\mu\text{m}^2$  and then study two more cases with different ligand affinities ( $K_d = 0.12$  and  $2.82\text{ nM}$ ), in addition to  $K_d = 0.76\text{ nM}$  case. The numbers of receptors brought to the brain side by vesicle are  $\sim 100$ ,  $90$ , and  $70$  respectively. As shown in Figure 7(a), for low affinity case ( $K_d = 2.82\text{ nM}$ ), the number of ligand-receptor bonds drops quickly to zero indicating the release of the particle from the membrane. When the ligand-receptor binding affinity is high ( $K_d = 0.12\text{ nM}$ ), compared with the lower affinity cases, the number of bonds drops slowly first and then reaches equilibrium with large number of bonds at  $\sim 50$ . As illustrated in Figure 6(d), the particle firmly binds inside the vesicle for high affinity case and the ligand-receptor bonds distribute uniformly around the particle, even at the neck region. As a result, the fusion pore size is significantly smaller than low affinity cases as shown in Figure 7(b). At equilibrium, the diameter of the pore at the neck is still not large enough for the release of particle. In this case, both the ligand-receptor affinity and the number of receptors contribute to the high particle avidity at the brain side.

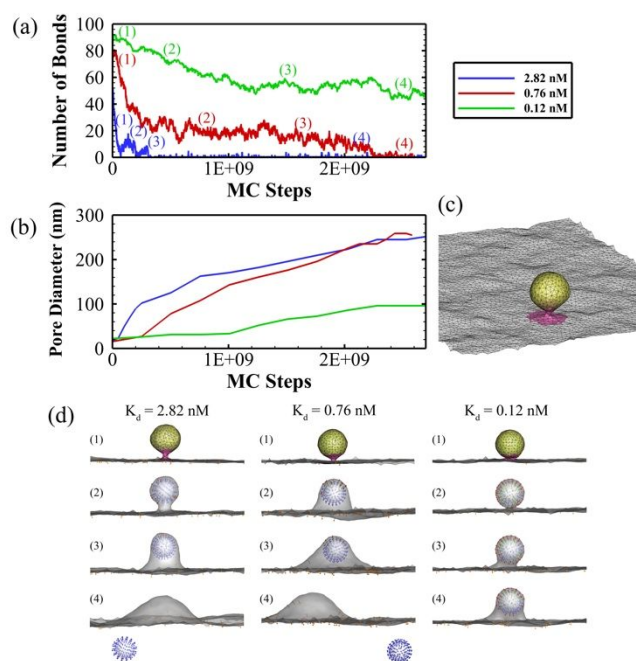


**Figure 7.** Effect of ligand-receptor binding affinity on exocytosis. (a) The number of ligand-receptor bonds formed during the MC simulations. (b) The diameter of the fusion pore during the MC simulation. (c) The top view of the fused vesicle and the membrane complex before pore opening. (d) The evolution of the profiles of the membrane-particle system at ligand-receptor affinity  $K_d = 0.12$ ,  $0.76$ , and  $2.82\text{ nM}$ . The actin induced tension (yellow region), actin induced force (pink region), bonded receptor (red dots), free receptor (black dots), bonded ligand (green dots) and unbonded ligand (blue dots) are all shown in the profiles.

### 3.5 Effect of actin assembly on exocytosis

The assembly of filamentous actin plays key roles in mediating the membrane fusion and pore expansion during exocytosis process.<sup>38, 46-48</sup> A variety of experiments have been performed,

but the findings are rather scattered. It seems that the filamentous actin is playing variable functional roles depending on different conditions. For example, some experiments showed that the actin promoted the fusion pore expansion and helped the delivery of granules,<sup>49–51</sup> while other experiments showed that actin actually limited the access of exocytotic granules to cell membrane.<sup>52, 53</sup> Moreover, Wen *et al.*<sup>54</sup> have shown that the assembly of filamentous actins provides sufficient membrane tension to facilitate the vesicle fusion in endocrine cells and neurons. On the other hand, actin dynamics inhibition is observed in virus-induced cell fusion<sup>55, 56</sup> and *Drosophila* myoblast fusion.<sup>57</sup>

In our model, the effects actin assembly have been represented by an increased tension on the vesicle and an extra force at the rim of the vesicle (see Methods section). We set up our simulations to study the effects of actin induce tension during fusion pore expansion. The ligand density and ligand-receptor binding affinity are fixed at  $5300 \mu\text{m}^2$  and  $0.76 \text{ nM}$ . It has been reported that the membrane tension is able to reach  $1\sim 3 \text{ pN/nm}$  during fusion pore expansion.<sup>58</sup> Therefore, we carry out simulations by varying the value of actin induced tension  $\sigma_{actin}$  from  $0.001$  to  $2.0 \text{ pN/nm}$ .<sup>59</sup>  $\sigma_{actin} = 0.04 \text{ pN/nm}$  has been adopted in our previous simulations (case with red color in Figure 6 and 7). As shown in Figure 8(a), decreasing the tension does not have much effect, but increasing the tension to  $0.2 \text{ pN/nm}$  shows clear impact. The number of ligand-receptor bonds quickly drops to zero within  $0.6e9$  MC steps, which is much faster than  $\sigma_{actin} = 0.04 \text{ pN/nm}$  case. As a result, the particle detaches from the membrane at a much earlier stage as illustrated in Figure 8(c). However, as we further increase the tension to a much higher level ( $\sigma_{actin} = 1.0$  and  $2.0 \text{ pN/nm}$ ), the ligand-receptor bonds immediately drops to zero, but the particle is completely wrapped by the membrane throughout the simulations (Figure 8(b)).

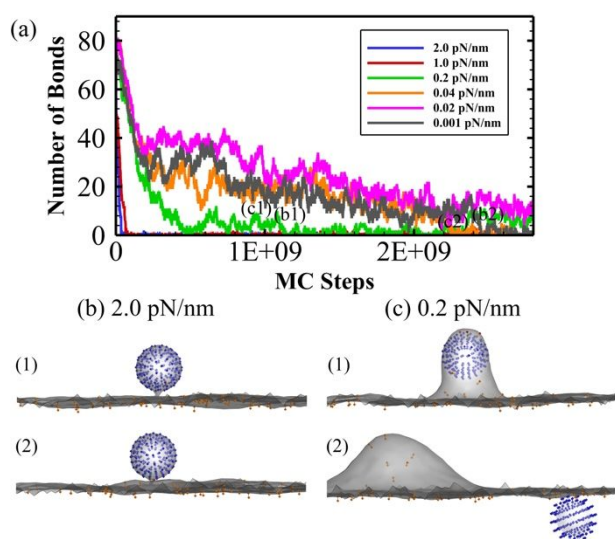


**Figure 8.** Effect of actin induced tension on exocytosis. (a) The number of ligand-receptor bonds formed during the MC simulations under different actin induced tension ( $\sigma_{actin}$ ). (b) The membrane-particle profiles at different stages for  $\sigma_{actin} = 2.0 \text{ pN/nm}$  and (c)  $\sigma_{actin} = 0.2 \text{ pN/nm}$ . The bonded receptor (red dots), free receptor (orange dots), bonded ligand (green dots) and unbonded ligand (blue dots) are all shown in the profiles.

Our results indicate that within a certain range, the actin induced tension facilitates the fusion pore expansion and particle release. But above certain value the tension tends to limit the pore expansion and inhibit the particle release. The particle release process is dictated by the competing factors, such as particle-membrane interactions, actin induced parallel force and actin induced tension. The compression from the tension has two impacts: First the compressive force will cause breakage of the ligand-receptor bonds and reduce of the particle-membrane interactions. Also, the shrinkage of vesicle tends to wrap around and lock the particle preventing it from release. Therefore, intermediate tension promotes while high tension inhibits the particle release from the brain side of BBB. The experiments from Muallem *et al.*<sup>49</sup> showed that in nonexcitable, cells the exocytosis cannot occur without certain actin cytoskeletal structure, but more actin network acted as a negative clamp blocking the exocytosis. This is consistent with our simulations. However, if the vesicle contains fluid phase cargo instead of particle, the second effect will not exist and we expect that the actin induce tension will promote the membrane fusion, as observed by Wen *et al.*<sup>54</sup>

## 4 Conclusions

The interaction between the nanoparticle and soft membrane during the receptor-mediated transcytosis is a complex and multi-step process. This highly complex process is dictated by various events, such as particle transport, receptor diffusion, membrane deformation, protein-protein and protein-membrane interactions. In addition to the physical and chemical effects, various biological components may involve during this process. Therefore study of RMT is significantly challenging. Here in this work, we have developed a stochastic model for investigation of the endocytosis and exocytosis processes during receptor-mediated transcytosis in the context of the transport of nanoparticles. The assembly of clathrin coated pit and filamentous actin have been accounted for in the endocytosis and exocytosis models respectively.

We have implemented our model to study the effect of particle avidity on both endocytosis and exocytosis. Both the ligand density and ligand-receptor binding affinity have been considered. Our results showed that there exists an optimal ligand density range that allows the particle to penetrate the cell. Higher ligand density always facilitates the endocytosis but may reduce the exocytosis efficiency. Particle with high ligand density forms more bonds at internalization side keeping it on the membrane surface. The ligand-receptor affinity has a similar effect. For a particle with fixed ligand density, the ligand-receptor affinity must be high enough for internalization, but the affinity needs to be lower than certain value for effective release. The results are consistent with the experimental work of Yu *et al.*<sup>16</sup> and Wiley *et al.*<sup>17</sup> In addition, through our model we have also investigated the functional roles of filamentous actin during fusion pore expansion and particle release. Interestingly the results showed that, the compression effect from actin induced tension tended to break the ligand-receptor

bonds facilitating the particle release, and to squeeze the particle blocking the release. Therefore, an intermediate tension promotes pore expansion and particle release, while high tension prohibits particle release. In summary, through this paper we have demonstrated that our model is able to provide deeper understanding of the fundamental mechanisms involved in receptor-mediated transcytosis. And our model represents a powerful platform for aiding the rational design of drug nanocarriers across biological barriers.

## Appendix A: Simulation parameters

The table below lists some of the simulation parameters used and the corresponding references:

**Table 1.** Some of the parameters used in the simulation

| Parameters  | Value                     | Ref    |
|---|---------------------------|--------|
| Size of membrane surface                                  | 910 nm × 910 nm           |        |
| Membrane bending rigidity $\kappa$                        | 20 $k_B T$                | 60     |
| Membrane characteristic tension $\sigma$                  | 0.001 pN/nm               | 61     |
| Actin induced tension at exocytosis site $\sigma_{actin}$ | 0.04 pN/nm                | 59     |
| Actin induced pressure at neck region $P$                 | 1 kPa                     | 39     |
| Clathrin bending rigidity $\kappa_{cla}$                  | 200 $k_B T$               | 62     |
| Clathrin intrinsic curvature $H_{cla}$                    | 0.036 nm <sup>-1</sup>    | 63     |
| Nanocarrier diameter                                      | 80 nm                     |        |
| Transferrin receptor length                               | 9.3 nm                    | 64     |
| Transferrin receptor radius                               | 5 nm                      | 64     |
| Ligand length   | 9 nm                      | 65     |
| Ligand radius   | 2.5 nm                    | 65     |
| Number of transferrin receptors on luminal side           | 300                       | 66     |
| Number of ligands per particle                            | 30 to 126                 | 17     |
| Equilibrium free energy change $\Delta G_0$               | -23 to -16 $k_B T$        | 16, 31 |
| Reactive compliance (reaction cut-off distance) $d_c$     | 0.9 nm                    | 31     |
| Receptor flexural rigidity $El$                           | 7000 pN · nm <sup>2</sup> | 67     |
| System temperature  | 298 K                     |        |

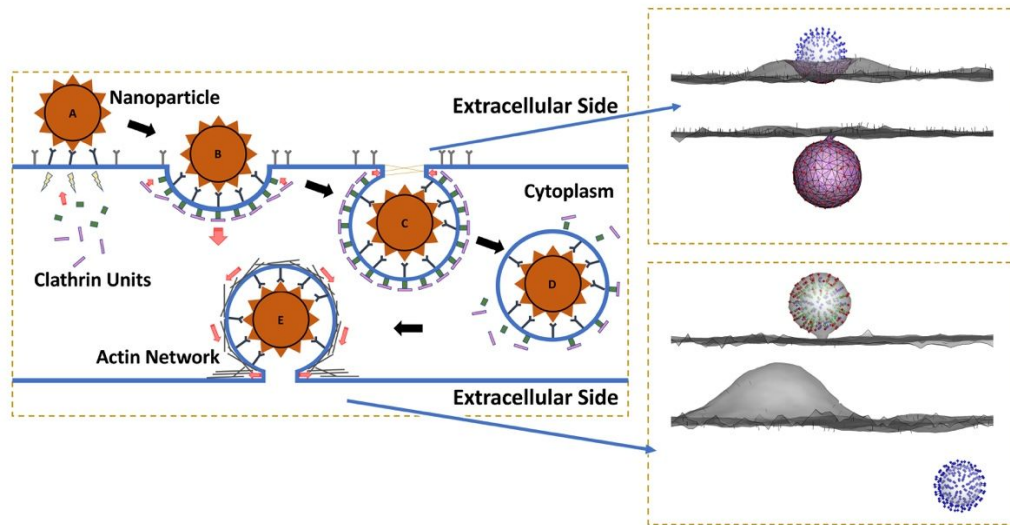
## Acknowledgements

Research reported in the publication was supported by the National Institute of General Medical Sciences of the National Institutes of Health under Award Number R01GM122081 and the National Science Foundation under CBET-1604211. Computational resources were provided in part by the Extreme Science and Engineering Discovery Environment (XSEDE) under grant No. MCB170012.

## References

- S. M. Tugizov, R. Herrera and J. M. Palefsky, *J. Virol.*, 2013, **87**, 8179-8194.
- R. C. McCarthy and D. J. Kosman, *Cell. Mol. Life Sci.*, 2015, **72**, 709-727.
- J. M. Lajoie and E. V. Shusta, *Annu. Rev. Pharmacol. Toxicol.*, 2015, **55**, 613-631.
- S. Tortorella and T. C. Karagiannis, *J. Membr. Biol.*, 2014, **247**, 291-307.
- J. Paterson and C. I. Webster, *Drug Discovery Today: Technologies*, 2016, **20**, 49-52.
- M. Bomsel, *Nat. Med.*, 1997, **3**, 42-47.
- L. Ouzilou, E. Caliot, I. Pelletier, M.-C. Prévost, E. Pringault and F. Colbère-Garapin, *J. Gen. Virol.*, 2002, **83**, 2177-2182.
- Y. Fujimura, M. Takeda, H. Ikai, K. Haruma, T. Akisada, T. Harada, T. Sakai and M. Ohuchi, *Virchows Arch.*, 2004, **444**, 36-42.
- S. M. Tugizov, R. Herrera, P. Veluppillai, D. Greenspan, V. Soros, W. C. Greene, J. A. Levy and J. M. Palefsky, *J. Virol.*, 2012, **86**, 2556.
- W. A. Banks, *Nature Reviews Drug Discovery*, 2016, **15**, 275.
- H. J. Gao, W. D. Shi and L. B. Freund, *Proc. Natl. Acad. Sci. U. S. A.*, 2005, **102**, 9469-9474.
- X. Yi and H. Gao, *Nanoscale*, 2017, **9**, 454-463.
- S. X. Sun and D. Wirtz, *Biophys. J.*, 2006, **90**, L10-L12.
- T. Yue and X. Zhang, *Soft Matter*, 2011, **7**, 9104-9112.
- J. REJMAN, V. OBERLE, I. S. ZUHORN and D. HOEKSTRA, *Biochem. J.*, 2004, **377**, 159-169.
- Y. J. Yu, Y. Zhang, M. Kenrick, K. Hoyte, W. Luk, Y. M. Lu, J. Atwal, J. M. Elliott, S. Prabhu, R. J. Watts and M. S. Dennis, *Sci. Transl. Med.*, 2011, **3**.
- D. T. Wiley, P. Webster, A. Gale and M. E. Davis, *Proc. Natl. Acad. Sci. U. S. A.*, 2013, **110**, 8662-8667.
- A. J. Clark and M. E. Davis, *Proc. Natl. Acad. Sci. U. S. A.*, 2015, **112**, 12486-12491.
- R. Vacha, F. J. Martinez-Veracoechea and D. Frenkel, *Nano Lett.*, 2011, **11**, 5391-5395.
- T. T. Yue and X. R. Zhang, *Soft Matter*, 2011, **7**, 9104-9112.
- H. M. Ding and Y. Q. Ma, *Biomaterials*, 2012, **33**, 5798-5802.
- H. Deng, P. Dutta and J. Liu, *Biochimica et Biophysica Acta (BBA) - General Subjects*, 2018, **1862**, 2104-2111.
- S. Sharma and M. Lindau, *Proceedings of the National Academy of Sciences*, 2018, **115**, 12751-12756.
- Y. Kozlovsky and M. M. Kozlov, *Biophys. J.*, 2002, **82**, 882-895.
- H. J. Risselada, C. Kutzner and H. Grubmüller, *ChemBiochem*, 2011, **12**, 1049-1055.
- P. M. Kasson, N. W. Kelley, N. Singhal, M. Vrljic, A. T. Brunger and V. S. Pande, *Proceedings of the National Academy of Sciences*, 2006, **103**, 11916-11921.
- R. Qiao, A. P. Roberts, A. S. Mount, S. J. Klaine and P. C. Ke, *Nano Lett.*, 2007, **7**, 614-619.
- K. Yang and Y.-Q. Ma, *Nat. Nanotechnol.*, 2010, **5**, 579.
- W. Helfrich, *Zeitschrift fuer Naturforschung Teil C Biochemie Biophysik Biologie Virologie*, 1973, **28**, 693-703.
- G. I. Bell, M. Dembo and P. Bongrand, *Biophys. J.*, 1984, **45**, 1051-1064.
- A. Yersin, T. Osada and A. Ikai, *Biophys. J.*, 2008, **94**, 230-240.
- A. Dautry-Varsat, A. Ciechanover and H. F. Lodish, *Proceedings of the National Academy of Sciences*, 1983, **80**, 2258-2262.

33. H. Sade, C. Baumgartner, A. Hugenmatter, E. Moessner, P. O. Freskgard and J. Niewoehner, *PLoS ONE*, 2014, **9**.
34. A. S. Haqqani, G. Thom, M. Burrell, C. E. Delaney, E. Brunette, E. Baumann, C. Sodja, A. Jezierski, C. Webster and D. B. Stanimirovic, *J. Neurochem.*, 2018, **146**, 735-752.
35. J. M. Trifaró, A. Rodríguez Del Castillo and M. L. Vitale, *Mol. Neurobiol.*, 1992, **6**, 339-358.
36. J.-M. Trifaró, S. Gasman and L. M. Gutiérrez, *Acta Physiol.*, 2008, **192**, 165-172.
37. N. Porat-Shliom, O. Milberg, A. Masedunskas and R. Weigert, *Cell. Mol. Life Sci.*, 2013, **70**, 2099-2121.
38. A. Papadopoulos, *Molecular and Cellular Neuroscience*, 2017, **84**, 93-99.
39. D. Manoussaki, W. D. Shin, C. M. Waterman and R. S. Chadwick, *Sci. Rep.*, 2015, **5**, 12314.
40. D. Banerjee, A. P. Liu, N. R. Voss, S. L. Schmid and M. G. Finn, *Chembiochem*, 2010, **11**, 1273-1279.
41. Y. Kozlovsky and M. M. Kozlov, *Biophys. J.*, 2003, **85**, 85-96.
42. X. Cao, M. A. Surma and K. Simons, *Cell Res.*, 2012, **22**, 793.
43. T. Worzfeld and M. Schwaninger, *Journal of cerebral blood flow and metabolism : official journal of the International Society of Cerebral Blood Flow and Metabolism*, 2016, **36**, 340-362.
44. R. L. Roberts, R. E. Fine and A. Sandra, *J. Cell Sci.*, 1993, **104**, 521-532.
45. F. E. Johansen and C. S. Kaetzel, *Mucosal Immunol.*, 2011, **4**, 598.
46. L. M. Gutiérrez, in *International Review of Cell and Molecular Biology*, ed. K. W. Jeon, Academic Press, 2012, vol. 295, pp. 109-137.
47. V. M. Tomatis, A. Papadopoulos, N. T. Malintan, S. Martin, T. Wallis, R. S. Gormal, J. Kendrick-Jones, F. Buss and F. A. Meunier, *The Journal of Cell Biology*, 2013, **200**, 301-320.
48. F. A. Meunier and L. M. Gutiérrez, *Trends Neurosci.*, 2016, **39**, 605-613.
49. S. Muallem, K. Kwiatkowska, X. Xu and H. L. Yin, *The Journal of Cell Biology*, 1995, **128**, 589-598.
50. K. M. Valentijn, F. D. Gumkowski and J. D. Jamieson, *J. Cell Sci.*, 1999, **112**, 81-96.
51. O. Larina, P. Bhat, J. A. Pickett, B. S. Launikonis, A. Shah, W. A. Kruger, J. M. Edwardson and P. Thorn, *Mol. Biol. Cell*, 2007, **18**, 3502-3511.
52. K. Miyake, P. L. McNeil, K. Suzuki, R. Tsunoda and N. Sugai, *J. Cell Sci.*, 2001, **114**, 3487-3494.
53. C. Ehre, A. H. Rossi, L. H. Abdullah, K. De Pestel, S. Hill, J. C. Olsen and C. W. Davis, *American Journal of Physiology-Cell Physiology*, 2005, **288**, C46-C56.
54. P. J. Wen, S. Grenklo, G. Arpino, X. Y. Tan, H. S. Liao, J. Heureaux, S. Y. Peng, H. C. Chiang, E. Hamid, W. D. Zhao, W. Shin, T. Nareoja, E. Evergren, Y. H. Jin, R. Karlsson, S. N. Ebert, A. Jin, A. P. Liu, O. Shupliakov and L. G. Wu, *Nat. Commun.*, 2016, **7**.
55. A. Chen, E. Leikina, K. Melikov, B. Podbilewicz, M. M. Kozlov and L. V. Chernomordik, *J. Cell Sci.*, 2008, **121**, 3619-3628.
56. M. A. Wurth, R. M. Schowalter, E. C. Smith, C. L. Moncman, R. E. Dutch and R. O. McCann, *Virology*, 2010, **404**, 117-126.
57. B. E. Richardson, K. Beckett, S. J. Nowak and M. K. Baylies, *Development*, 2007, **134**, 4357-4367.
58. L. V. Chernomordik, G. B. Melikyan and Y. A. Chizmadzhev, *Biochimica et Biophysica Acta (BBA) - Reviews on Biomembranes*, 1987, **906**, 309-352.
59. M. M. Kozlov and L. V. Chernomordik, *Curr. Opin. Struct. Biol.*, 2015, **33**, 61-67.
60. E. Evans and W. Rawicz, *Phys. Rev. Lett.*, 1990, **64**, 2094-2097.
61. J. E. Hassinger, G. Oster, D. G. Drubin and P. Rangamani, *Proceedings of the National Academy of Sciences*, 2017, **114**, E1118-E1127.
62. A. J. Jin, K. Prasad, P. D. Smith, E. M. Lafer and R. Nossal, *Biophys. J.*, 2006, **90**, 3333-3344.
63. S. Zaremba and J. H. Keen, *The Journal of Cell Biology*, 1983, **97**, 1339-1347.
64. H. Fuchs, U. Lücken, R. Tauber, A. Engel and R. Geßner, *Structure*, 1998, **6**, 1235-1243.
65. H. M. Berman, J. Westbrook, Z. Feng, G. Gilliland, T. N. Bhat, H. Weissig, I. N. Shindyalov and P. E. Bourne, *Nucleic Acids Res.*, 2000, **28**, 235-242.
66. J. D. Bleil and M. S. Bretscher, *The EMBO Journal*, 1982, **1**, 351-355.
67. S. Weinbaum, X. B. Zhang, Y. F. Han, H. Vink and S. C. Cowin, *Proc. Natl. Acad. Sci. U. S. A.*, 2003, **100**, 7988-7995.



Stochastic model of clathrin-mediated endocytosis and actin-mediated exocytosis is developed for study of transcellular nanoparticle transport.